Immunopathol Persa. 2026;12(2):e43980 Case Report

Immunopathologia Persa

http immunopathol.com

DOI:10.34172/ipp.2025.43980

A novel gross deletion in SMARCAL1 impairs DNA replication fork regression, leading to severe Schimke immuno-osseous dysplasia; a literature review and an integrated study of clinical, genetic, and protein-protein interaction analysis

Mohammad Saberi[1], Morteza Talebi[2], Ali Ghorbani[3], Azadeh Reshadmanesh[4], Samin Sharafian[5], Zahra Chavoshzadeh[5], Masumeh Mohkam[6], Arefeh Zahmatkesh[7], Paniz Pourpashang[8,9*]

[1]Department of Medical Genetics, Faculty of Medicine, Tehran University of Medical Sciences, Tehran, Iran
[2]Department of Medical Genetics and Molecular Biology, Faculty of Medicine, Iran University of Medical Sciences, Tehran, Iran
[3]Protein Research Center, Shahid Beheshti University, Tehran, Iran
[4]Department of Medical Biotechnology, Faculty of Medical Sciences, Tarbiat Modares University, Tehran, Iran
[5]Department of Immunology and Allergy, Mofid Children's Hospital, Shahid Beheshti University of Medical Sciences, Tehran, Iran
[6]Pediatric Nephrology Research Center, Shahid Beheshti University of Medical Sciences, Tehran, Iran
[7]School of Medicine, Shahid Beheshti University of Medical Sciences, Tehran, Iran
[8]Pediatric Chronic Kidney Disease Research Center, Gene, Cell and Tissue Research Institute, Tehran University of Medical Sciences, Tehran, Iran
[9]Department of Pediatric Nephrology, Bahrami Hospital, School of Medicine, Tehran University of Medical Sciences, Tehran, Iran

***Correspondence to**
Paniz Pourpashang, Email: paaniz.p@gmail.com, p-pourpashang@sina.tums.ac.ir

Received 16 Aug. 2025
Revised: 31 Oct. 2025
Accepted 1 Nov. 2025
ePublished 9 Nov. 2025

Abstract

Schimke immuno-osseous dysplasia (SIOD) is an exceptionally rare autosomal recessive disorder that affects multiple organ systems, most notably the skeletal system, kidneys, and immune system. The clinical manifestations of SIOD include growth retardation, skeletal deformities, progressive proteinuria, and immunodeficiency. Severe cases may progress to nephrotic syndrome and cerebral infarctions. The disorder is primarily attributed to biallelic mutations in the *SMARCAL1* gene, which leads to the early onset of symptoms and often results in premature mortality. In this study, we identified a novel gross deletion encompassing exons 5 and 6 of the *SMARCAL1* gene. This deletion leads to a partial loss of the HARP1 and HARP2 domains and the generation of a novel HARP domain that is structurally similar to both HARP1 and HARP2, while retaining conserved amino acids. Our AlphaFold 3D modeling indicated that the truncated *SMARCAL1* protein is identical to the wild-type *SMARCAL1*, except for the absence of HARP1 domain, and resembles invertebrate *SMARCAL1*, which naturally possesses only one HARP domain. Previous studies have demonstrated that human *SMARCAL1* lacking the HARP1 domain retains normal helicase, ATPase, and DNA-binding activities. Additionally, invertebrate *SMARCAL1*, which also lacks the HARP1 domain, fails to effectively regress DNA replication forks. This suggests that the identified gross deletion may contribute to SIOD pathogenesis by impairing DNA replication fork regression and genomic instability.

Keywords: Focal segmental glomerulosclerosis, Schimke immuno-osseous dysplasia, SMARCAL1, Mutational analysis, 3D protein modeling, Protein-DNA interaction

Citation: Saberi M, Talebi M, Ghorbani A, Reshadmanesh A, Sharafian S, Chavoshzadeh Z, Mohkam M, Zahmatkesh A, Pourpashang P. A novel gross deletion in SMARCAL1 impairs DNA replication fork regression, leading to severe Schimke immuno-osseous dysplasia; a literature review and an integrated study of clinical, genetic, and protein-protein interaction analysis. Immunopathol Persa. 2026;12(2):e43980. DOI:10.34172/ipp.2025.43980.

Introduction

Schimke immuno-osseous dysplasia (SIOD) is an exceedingly rare condition with an incidence rate of 1-3 cases per million births, and it is inherited in an autosomal recessive manner (1). The hallmark of this disease is the involvement of multiple organs, notably affecting the skeletal system, kidneys, and immune system. Clinical presentations commonly encompass stunted growth, skeletal abnormalities, progressive proteinuria, intermittent lymphopenia, and impaired cellular immunity leading to varying degrees of deterioration (2). Severe manifestations may encompass bone marrow insufficiency and potentially fatal cerebral vascular complications (3–5). The critical manifestation of SIOD frequently emerges prenatally or within the initial 2 to 5 years of existence, distinguished by life-threatening nephrotic manifestations and cerebral infarctions. Severe phenotypes commonly lead to premature mortality, notably after end-stage renal disease (1,5,6).

Most individuals diagnosed with SIOD typically exhibit renal impairment, initially manifesting as proteinuria, evolving into steroid-resistant nephrotic syndrome,

Key point

Schimke immuno-osseous dysplasia (SIOD) is an exceptionally rare autosomal recessive disorder that affects multiple organ systems, most notably the skeletal system, kidneys, and immune system. The clinical manifestations of SIOD include growth retardation, skeletal deformities, progressive proteinuria, and immunodeficiency. Severe cases may progress to nephrotic syndrome and cerebral infarctions. In this study, we identified a novel gross deletion encompassing exons 5 and 6 of the *SMARCAL1* gene.

and eventually advancing to end-stage renal disease necessitating either dialysis or renal transplantation. Analysis of renal cells from SIOD patients has revealed elevated levels of DNA fragmentation, commonly associated with focal segmental glomerulosclerosis (FSGS), and minimal alterations in disease histopathology (3). Moreover, an additional prevalent discovery present in 80% of individuals is a modification in immune cells that makes them more susceptible to repeated bacterial, viral, or fungal infections (4). Therefore management of these individuals necessitates the use of preventative measures, while considering the diverse manifestations of the disease (3).

SIOD arises from biallelic mutations in the *SMARCAL1* gene also known as HARP (HepA- related protein) or HHARP situated on chromosome 2q34-q36. This gene encodes two distinct transcripts, NM_001127207.2 and NM_014140.4, which differ in their 5' untranslated regions (UTRs). Both transcripts, however, encode the same *SMARCAL1* protein, comprising 954 amino acid residues and classified within the SWI/SNF protein family (7). Proteins in this family are known for their helicase and ATPase functions and are believed to influence the transcription of specific genes by modifying the chromatin structure surrounding them (8). This protein has been known to play a pivotal role in replication fork stabilization and genome integrity (6). Replication forks are generated during DNA replication as helicases unwind the double-stranded DNA at origins of replication, creating single-stranded DNA templates for DNA polymerase (9). This process involves coordinated leading and lagging strand synthesis. However, replication forks are frequently challenged by obstacles, including DNA lesions, secondary structures, or protein-DNA complexes, which can stall fork progression (10). Stalled forks lead to the accumulation of ssDNA compromising genomic integrity by exposing it to nuclease-mediated cleavage, thereby significantly increasing the likelihood of genetic rearrangements (11–13). Insufficient stabilization of stalled replication forks can lead to the disassembly of the replisome and subsequent degradation or collapse of the fork. In human cells, the accumulation of replication protein A (RPA), a single-stranded DNA-binding protein, at these stalled forks indicates the recruitment of ATR, a key S-phase checkpoint kinase (14,15). This event triggers the recruitment of additional proteins that are involved in sister chromatid cohesion and the stabilization of the histone/chromatin structure (16). To address stalled forks, mechanisms such as regression into a four-stranded 'chicken foot' structure can occur, where nascent DNA strands are unwound from their leading and lagging strand templates and subsequently reannealed (16). SMARCAL1, which preferably binds to branched DNA structures, is crucial for maintaining genomic stability by preventing genetic rearrangements and facilitating DNA repair. It functions by stabilizing replication forks and promoting fork regression, thereby mitigating the impact of DNA lesions (13).

The human *SMARCAL1* protein comprises an RPA binding domain, a helicase ATP-binding domain, a helicase C-terminal domain, and two HARP domains. These domains are characterized by highly conserved residues across vertebrates and invertebrates (Figure 1).

While vertebrate SMARCAL1 proteins contain two HARP domains, invertebrate counterparts possess only one (13). Mutations in conserved residues within these SMARCAL1 domains have been implicated in the development of SIOD disease (17). Although HARP1 and HARP2 domains are highly conserved both within and across species, they serve distinct functions. HARP2 is crucial for DNA binding, ATPase activity, and annealing helicase functions, whereas HARP1 appears to play a more

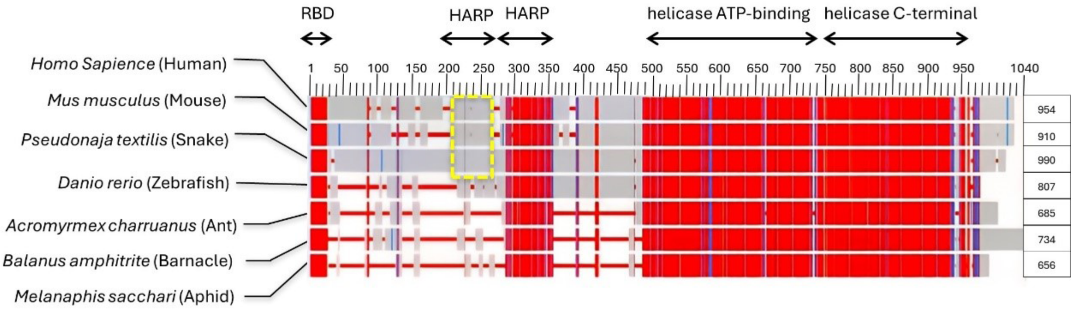

Figure 1. Conservation of SMARCAL1 domains across vertebrate and invertebrate species. The SMARCAL1 protein in vertebrates is characterized by five domains: an RPA binding domain (RBD), two HARP domains, a helicase ATP-binding domain, and a helicase C-terminal domain. In contrast, invertebrate SMARCAL1 proteins lack one of the HARP domain repeats present in vertebrates (yellow box). Despite this difference, SMARCAL1 proteins across both vertebrate and invertebrate species exhibit highly conserved residues (highlighted in red).

supportive role in facilitating *SMARCAL1* activity (18). In human SMARCAL1, HARP1 is encoded by exons 3, 4, and 5, while HARP2 is encoded by exons 5, 6, and 7 (19).

A significant challenge in modern genetics lies in predicting the functional consequences of the vast array of variants identified through large-scale sequencing efforts. This is particularly crucial for evaluating variants in the human genome that may play a role in disease pathogenesis (20). Several computational tools, such as MutationTaster (21), Condel (22), and Sorting Intolerant From Tolerant (SIFT) (23), have been developed to prioritize potentially deleterious variants. However, a notable limitation of these sequence-based approaches is their inability to elucidate the specific mechanisms through which amino acid substitutions, deletions, or insertions disrupt protein structure, potentially leading to disease (20). Structure-based predictive methods, by contrast, offer more comprehensive and reliable insights into the molecular consequences of missense, nonsense and indel mutations on protein conformation and their role in disease causality (19,24,25).

Advanced computational approaches, including Swiss-Model, Phyre2, IntFOLD, and I-TASSER, often utilize homology modeling for prediction of protein tertiary structures, which relies on existing experimentally derived structures as templates. The underlying principle of these models is that proteins with high sequence similarity are likely to share similar three-dimensional structures (26–28). AlphaFold 3 (AF3), released in 2024 by Google DeepMind, has set a new benchmark in protein structure and protein-interaction prediction, surpassing even experimental methods (29).

In our investigation, we discovered a homozygous large deletion accompanied by a 21-nucleotide insertion in the *SMARCAL1* gene, marking a significant finding in understanding SIOD. Our approach began with employing single nucleotide variations and copy number variations (CNV) analysis tools to detect the disease-causing variant in a patient exhibiting SIOD-related clinical features. We also reviewed all pathogenic or likely pathogenic variants listed in available databases, and relevant literature to understand their distribution and location within functional domains. Finally, Utilizing AF3, we explored how the novel gross deletion affects the 3D structure of SMARCAL1 and its interaction with a simulated DNA replication fork, offering the first comprehensive analysis of the effects of truncating mutations on SMARCAL1's structural integrity and functionality in silico.

Case Presentation and Clinical Assessment

In November 2022, a 9-year-old female from a consanguineous marriage, with comprehensive medical documentation was referred to the Bonyan medical genetic laboratory (Tehran, Iran), with a potential diagnosis of combined immunodeficiency with nephropathy. Before this referral, various clinical evaluations such as routine laboratory examinations, ultrasound assessments, kidney and bone marrow biopsies, and rheumatology and immunology screenings had been conducted. Findings of these evaluations are extensively discussed in the results section. After thorough genetic counseling and the creation of family pedigree (Figure 2), the patient's parents provided written consent for whole exome sequencing (WES) to be performed.

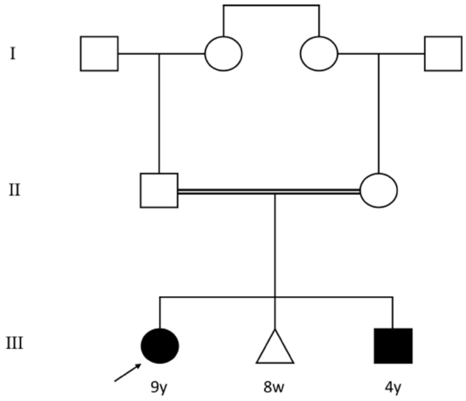

Figure 1. Pedigree of the consanguineous family. The proband is highlighted with an arrow. The proband's mother had a previous record of experiencing a single miscarriage occurring at eight weeks. Furthermore, the sibling of the proband exhibits similar symptoms to those of the proband.

Whole exome sequencing

A whole blood sample was obtained from the patient, and an assessment of the sample's quality was conducted. WES was performed by CeGat (Tübingen, Germany) and exons were captured using Twist Exome Target Enrichment Kit. This was followed by a paired-end high-throughput sequencing conducted on the Illumina NovaSeq 6000 platform, manufactured by Illumina Inc, with an average sequencing depth of 299X. Quality control assessment of the generated FastQ files was carried out using FastQC software. Subsequently, the paired reads underwent alignment to the human reference genome (hg19) through the utilization of the Burrows-Wheeler Aligner. Duplicate reads were identified and annotated using PICARD tools. The GATK Unified Genotyper and GATK-gCNV modules were employed to perform tasks such as Indel realignment, base recalibration, variant calling, and variant filtering. The variants were annotated using the SnpEff and SVAnnotate tools, following these steps. The identified variants' prioritization was conducted by considering various factors, including population frequency, the impact or characteristics of the variants, and zygosity.

NGS based CNV-calling

Copy number variations were determined through the analysis of uniquely mapped, non-duplicated, high-quality sequencing reads using an in-house developed approach rooted in sequencing coverage depth. In essence, a model reflecting wet-lab biases and between-sample differences was constructed based on reference samples to represent the anticipated coverage. The identification of CNVs entailed the computation of the sample's standardized coverage profile alongside its departure from the projected coverage. Genomic regions were called variants if they deviate significantly from the expected coverage.

Variant confirmation

Quantitative polymerase chain reaction (qPCR) was conducted to assess the dosage of the deleted region compared to the *ALB* (Albumin) gene in both parents and the patient. The qPCR assay was carried out using RealQ Plus 2x Master Mix Green (Amplicon™, Denmark) and *SMARCAL1*- exon 6-specific primers, within a total reaction volume of 15 µl. The qPCR procedure was performed utilizing the Step One Plus Real-Time PCR System by Applied Biosystems in the following sequence: initial denaturation at 95 °C for 5 minutes, followed by 40 cycles of denaturation at 95 °C for 10 seconds, primer annealing at 58 °C for 10 seconds, elongation at 72 °C for 10 seconds, and a final extension at 72 °C for 1 minute.

Furthermore, the boundaries of the deleted genomic region were identified by employing a primer walking approach, using specific primers that marked the breakpoints as follows: Forward Primer: 5' GCATGGTGACTTAGATGACTTCTGC 3', Reverse Primer: 5' AAAGGCTAATCGTCCTCCGGTATC 3'. The PCR protocol consisted of an initial denaturation step at 95 °C for 5 minutes, 40 cycles of denaturation at 95 °C for 40 seconds, primer annealing at 66 °C for 30 seconds, elongation at 72 °C for 2 minutes, and a final extension at 72 °C for 10 minutes. Ultimately, bidirectional Sanger sequencing was executed employing both forward and reverse primers at a reading temperature set at 66 °C.

Database analysis and literature review

The pathogenic and likely pathogenic variants in the *SMARCAL1* gene, previously documented in the literature, ClinVar, and HGMD databases, were compiled. The functional domains of the *SMARCAL1* gene were determined through the Uniprot database and subsequently depicted according to their positions in the protein structure. Finally, the distribution of variants across these functional domains was visualized.

Bioinformatic studies and 3D modeling

To assess the impact of the gross deletion (exons 5 and 6) on the *SMARCAL1* amino acid sequence, we utilized the NCBI Sequence Viewer. The Illustrator for Biological Sequences (IBS) tool was used to visually represent the deleted regions on the *SMARCAL1* protein (30). The potential frameshifting in the amino acid sequence was examined and the remaining residues were incorporated to generate a truncated *SMARCAL1* variant. Protein domain analysis was performed using InterProScan (31) to identify the specific domains affected by the deletion.

To evaluate the impact of the gross deletion on the 3D structure of *SMARCAL1*, we modeled the 3D structures of wild-type human SMARCAL1 (hwSMARCAL1), truncated human SMARCAL1 (htSMARCAL1), and the wild-type SMARCAL1 from Melanaphis sacchari (msSMARCAL1), an invertebrate model species, using AF3. The models were compared through 3D pairwise alignment using UCSF ChimeraX (32-34). To facilitate comparison, the RBD and the subsequent long-disordered region were removed from the amino acid sequences of these models.

To determine if the gross deletion compromises the interaction between SMARCAL1 and the DNA replication fork, we conducted a 3D simulation of this interaction using AF3 for hwSMARCAL1, htSMARCAL1, and msSMARCAL1. AF3 has been previously validated for its accuracy in modeling protein-DNA interactions (29) and we further validated its performance specifically for modeling protein-DNA replication fork interactions. To achieve this, we re-modeled the interaction between RecG and a three-way DNA replication fork (PDB 1GM5), for which the interaction has been determined by X-ray diffraction (35). The sequences of RecG and the three-way DNA replication fork, including ADP and Zn^{2+}, were introduced into AF3 to evaluate its capability to reproduce the experimentally determined 3D interaction.

Following this validation, a similar simulation was performed for the three SMARCAL1 variants against a virtual DNA replication fork, designed based on previous studies. We compared the interactions of the three SMARCAL1 variants with the virtual DNA replication fork using pLDDT scores. For all models in this study, three replicates were conducted, with the seed set to maximum in AF3. The model with the highest pLDDT score and, where applicable, the highest ipTM score, was considered the best model.

Results

Clinical findings and medical procedures

The patient was delivered via cesarean section at 34 weeks of gestation due to oligohydramnios and required neonatal intensive care unit (NICU) stay. Initial evaluation in the NICU indicated elevated serum creatinine levels and electrolyte imbalances, necessitating urgent hemodialysis, followed by routine peritoneal dialysis (Table 1).

A renal ultrasound scan revealed a unilateral ectopic kidney. Subsequently, the patient presented with loss of consciousness, proteinuria, and severe peripheral edema, prompting treatment with losartan and prednisolone to address elevated urinary protein-creatinine ratio, hypoalbuminemia, and periorbital edema. Administration of albumin alleviated the edema. Despite short stature, with no significant bone deformity or congenital anomalies were evident upon clinical examination. Seizures occurred during dialysis, necessitating treatment with sodium valproate. Pancytopenia was observed in

Table 1. General hematology and biochemistry tests results

Test	Result	Unit	Reference value
WBC	1.2	Cells/µL	$4\text{-}11 \times 10^3$
RBC	4.35	Cells/µL	Male $4.5\text{-}5.9 \times 10^6$, Female $4.5\text{-}5.1 \times 10^6$
Hgb	11	g/dL	Male 14.5-17.5, Female 12.3-15.3
Hct	42.1	%	Male 41.5-50.4, Female 36-44.6
PLT	115	$\times 10^3$/ µL	$150\text{-}450 \times 10^3$
MCV	96.8	fl	80-96
MCH	32.2	Pg	27.5-33.2
MCHC	33.3	g/dL	33.4-35.5
RDW	15.3	fL	11.6-14.6
Urea	203	mg/dL	1-3 years: 11-36 4-13 years: 15-36 14-19 years: 18-45 20-50 years female: 15-40 >50-year female: 21-43 20-52 years male: 19-44 >52 years:18-55
Creatinine	**5**	mg/dL	Male: 0.7-1.4 Female: 0.6-1.3
Na	135	meq/L	135-145
K	3.8	meq/L	3.5-5
Ca	7.8	mg/dL	Newborn: 8-13 1 year-90 years: 8.5-10.5
Mg	1.8	mg/dL	Newborn: 1.2-2.6 Child: 1.5-2.3 Female: 1.9-2.5 Male: 1.8-2.6
Albumin	2.8	g/dL	3.5-5.2
Phosphorus	7.2	mg/dL	Newborn (1-30 days): 3.9-7.7 Newborn (1-12 months): 3.5-6.6 Newborn (1-30 years): 3.1-6 Baby (4-6 years): 3.3-5.6 Baby (7-9 years): 3-5.4 Baby (10-12 years): 3.2-5.7 Baby (13-15 years): 2.9-5.1 Baby (16-18 years): 2.7-4.9 Adults: 2.6-4.5

WBC: White blood cell, RBC: Red blood cell, Hgb: Hemoglobin, Hct: Hematocrit, PLT: Platelet, MCV: Mean corpuscular volume, MCH: Mean corpuscular hemoglobin, MCHC: Mean corpuscular hemoglobin concentration, RDW: Red cell distribution width, Na: Serum sodium, K: Serum potassium, Ca: Serum calcium, Mg: Serum magnesium.

laboratory findings, initially suspected to be related to COVID-19 infection due to coryza symptoms but later ruled out by negative COVID-19 PCR testing. Atypical manifestations of autoimmune hematological diseases such as hemolytic uremic syndrome (HUS) and thrombotic thrombocytopenic purpura (TTP) were considered but excluded based on normal rheumatology evaluation and HUS panel results (Table 2).

Adverse effects of sodium valproate were also considered. Given diagnostic uncertainties, a kidney biopsy revealed chronic tubulointerstitial damage. Despite persistent pancytopenia, bone marrow biopsy results were normal. Upper endoscopy conducted due to ongoing abdominal pain detected esophageal candidiasis. An immunological panel identified combined immunodeficiency (Tables 3-4).

Genetic findings

A homozygous CNV spanning approximately 3 kb, with a potential pathogenic implication was detected on chromosome 2. The CNV encompassed exons 5 and 6 of the *SMARCAL1* gene**.** Then, qPCR analysis was conducted to evaluate the exon 6 dosage relative to the *ALB* gene in both parents and the patient. In addition, qPCR analysis shows a homozygous deletion of exon 6 in the patient and a heterozygous status in the parents compared to the normal control. Following multiple steps of primer walking, the exact deletion site was pinpointed, involving the replacement of 21 nucleotides. The identified insertion-deletion variant was named according to the Human Genome Variation Society (HGVS) as c.862+1760_1148-729delinsCACACCAGCACATCTGGCTAA, representing a large deletion spanning exons 5 and 6 of the *SMARCAL1*

Table 2. Lymphocyte transformation test

Test	Patient's SI	Control's SI	Normal range
LTT-PHA	1.3	8.6	>3
LTT-BCG	1	2.5	>2.5

LTT-PHA: Lymphocyte transformation test with phytohemagglutinin, LTT-BCG: Lymphocyte transformation test with Bacillus Calmette-Guerin.

Table 3. Immunoglobulin response

Test	Result	Method	Reference
Diphtheria Ab (IgG)	0.01 IU/mL	ELISA	<0.01: No protection. 0.01-0.1: No reliable protection, Booster vaccination is recommended.
Tetanus Ab (IgG)	0.1 IU/mL	CLIA	>0.10: Adequate immune protection.

Ab: Antibody, CLIA: Chemiluminescence immunoassay; ELISA: Enzyme-linked immunosorbent assay.

Table 4. Lymphoproliferative panel

Test (Blood)	Result	Reference value
CD3	24%	35-78
CD19	15%	3-14
CD20	14%	3-15
CD45RO (CD4)	83%	13-30
CD45RA (CD4)	11%	46-77
CD45RA (CD8)	75%	63-92
CD45RO (CD8)	%3%	4-21
CD16+CD56	6.78%	4-17

CD3: Clusters of differentiation 3.

gene, with a 21-bp insertion (Figure 3). Finally, the presence of this variant was also detected in the affected brother with distinct clinical manifestations.

Database analysis and literature review

Based on our investigation, a total of 77 pathogenic and likely pathogenic variants within the *SMARCAL1* gene have been documented in databases such as ClinVar and HGMD, as well as in the published articles. A missense variant (p.Ser585Phe) was reported previously in an 8 years old male with generalized edema, kyphosis, and nephrotic syndrome (36). Other variants in ClinVar and HGMD databases illustrated in Figure 4. These variants comprise 16 frameshifts, 24 missense, 16 nonsense, 20 mutations affecting splicing. Among these, two variants are situated within the RBD, one variant is located within the HARP1 domain, seven variants are within the HARP2 domain, eleven variants are within the Helicase ATP binding domain, and eleven variants are within the Helicase C-terminal domain. Notably, the concentration of missense mutations is observed in the region between the two terminal domains, highlighting the significance of this region in protein folding.

Bioinformatics and 3D modeling findings

In our experimental study, we confirmed that the novel gross deletion led to the complete excision of exons 5 and 6 (Figure 5A). Furthermore, the insertion of 21 nucleotides did not affect the amino acid sequence, as these nucleotides were incorporated into the intronic region between exons 4 and 7. At the transcript level, the deletion of exons 5 and 6 resulted in the rejoining of the adenosine residue at the end of exon 4 with the two thymidines at the beginning of exon 7. This reconstitution restored the deleted ATT codon, which encodes the isoleucine residue (Figure 5B). Amino acid sequence analysis revealed that this non-frameshift mutation led to the deletion of 95 amino acids, spanning from M288 to L382, without introducing new

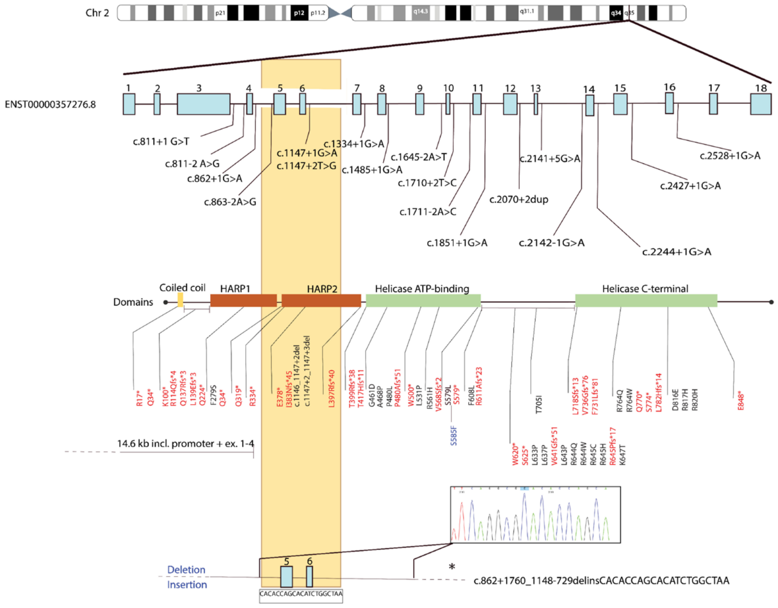

Figure 3. The dispersion of pathogenic and likely pathogenic variants within the functional domains of the *SMARCAL1* gene. The identified novel large deletion is highlighted with a yellow bar.

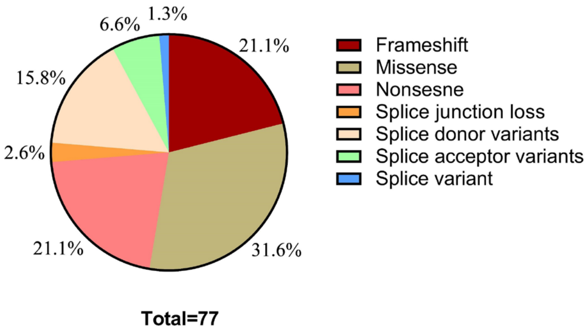

Figure 4. The proportion of each mutation type within the *SMARCAL1* gene.

amino acid residues.

Protein domain analysis indicated that the gross deletion removed 15 amino acids from the C-terminal end of the HARP1 domain, 40 amino acids from the N-terminal end of the HARP2 domain, and the entire 40 amino acid of the disordered region located between the HARP1 and HARP2 domains (Figure 5C). This resulted in the rejoining of the remaining segments of HARP1 (40 amino acids) and HARP2 (15 amino acids), thereby forming a novel HARP domain with a similar amino acid count and characteristic to the original HARP1 and HARP2 domains (Figure 5D).

3D structure predicted by AF3 revealed that the gross deletion results in the partial removal of the C-terminal alpha helix within the HARP1 domain and the complete removal of the HARP2 domain, except for the last portion of its C-terminal alpha helix. This alteration gives rise to a new HARP domain that mirrors the structural characteristics of both the original HARP1 and HARP2 domains (Figure 6A).

Sequence alignment of the fused HARP domain with the original HARP1 and HARP2 domains revealed that the new HARP domain retains the same conserved amino acids as HARP1 and HARP2 (Figure 6B). This finding indicates that the deletion of 95 amino acid residues does not compromise the conservation within the fused HARP domain; in contrast, it preserves the conserved sequences present in HARP1 and HARP2. Additionally, the 3D structure predicted by AF3 further supports this observation. The 3D model of the newly formed HARP domain was fully aligned with those of HARP1 and HARP2. This pairwise alignment demonstrated that the new HARP domain is structurally equivalent to both the HARP1 and HARP2 domains, suggesting that it may retain similar functional properties as well (Figure 6C).

Although the fused HARP domain may function similarly to either the HARP1 or HARP2 domains, it is possible that SMARCAL1 might not function optimally with only one single HARP domain. However, intra-species domain analysis using InterProScan and 3D structure predictions by AF3 indicated that SMARCAL1 in invertebrates, functions naturally with a single HARP domain (Figure 7). This suggests that human SMARCAL1 with the single fused HARP domain could theoretically retain functionality. The evolutionary reason for the acquisition of an additional HARP domain in vertebrates remains unclear; nevertheless, the presence of a single HARP domain in invertebrates supports the notion that human SMARCAL1 can function with just one HARP domain.

Supporting this notion, a recent study confirmed that the

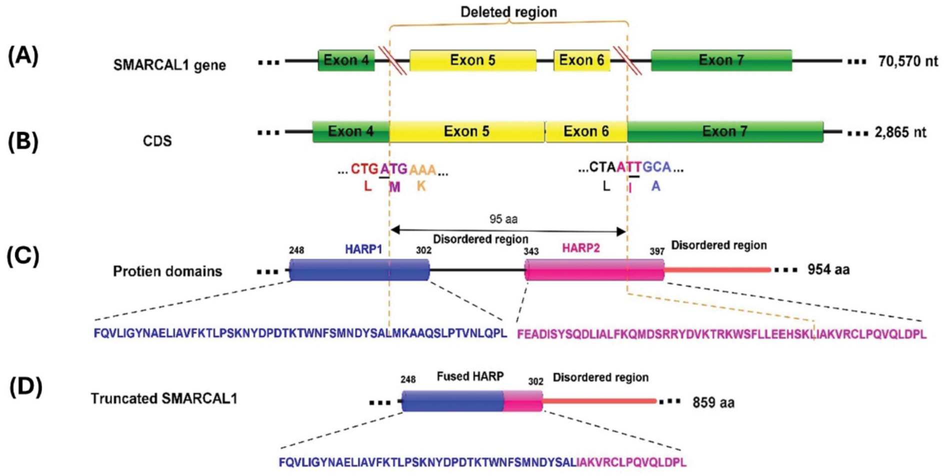

Figure 5. The Impact of the Gross Deletion on *SMARCAL1* Amino-acid Sequence. The gross deletion led to the complete removal of exons 5 and 6 **(A)**, resulting in the rejoining of the adenosine residue at the end of exon 4 with the two thymidines at the beginning of exon 7 (underlined in **(B)**). This reconstitution restored the deleted ATT codon, which encodes the isoleucine residue. At the protein level, this deletion removed 95 amino acids, including 40 amino acids from the N-terminal end of the HARP2 domain and the entire 40-amino-acid disordered region located between the HARP1 and HARP2 domains **(C)**. Consequently, this led to the formation of a new HARP domain, referred to as the fused HARP domain **(D)**. Furthermore, by the 3D structure predicted by Alphafold3, it is obvious that the gross deletion leads to the partial removal of the C-terminal alpha helix of the HARP1 domain and the complete loss of the HARP2 domain, with the exception of the partial retention of its C-terminal alpha helix. As a result, a new HARP domain is generated, which structurally resembles both the original HARP1 and HARP2 domains.

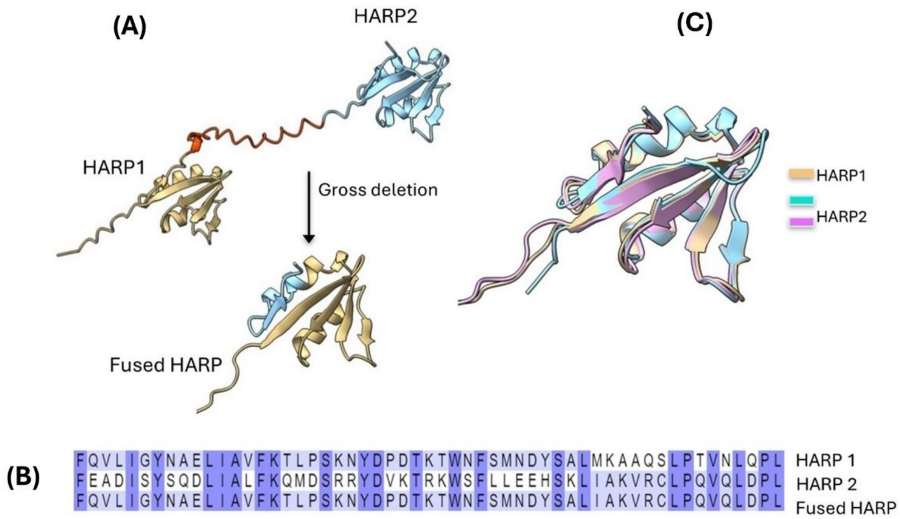

Figure 6. Generation of a new HARP domain after introduction of the gross deletion. The gross deletion causes the partial removal of the C-terminal alpha helix in the HARP1 domain and the complete removal of the HARP2 domain, except for the partial retention of its C-terminal alpha helix **(A)**. This deletion results in the formation of a new HARP domain that closely resembles the original HARP1 and HARP2 domains in terms of conservation **(B)** and 3D structure **(C)**.

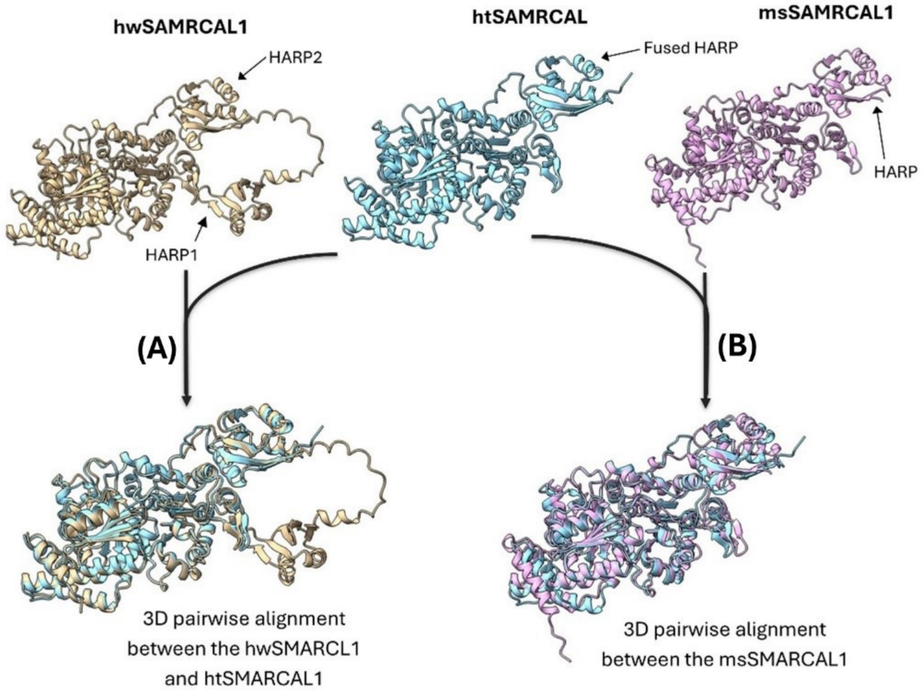

Figure 7. Three-dimensional alignment of htSMARCAL1 (cyan) with hwSMARCAL1 (gold) and msSMARCAL1 (violet). The 3D structure prediction using AlphaFold3 demonstrates that htSMARCAL1 is structurally identical to hwSMARCAL1, except for the absence of the HARP1 domain. Additionally, the 3D structure of htSMARCAL1 shows a high degree of alignment with msSMARCAL1, particularly within their HARP domains.

complete deletion of HARP1 in human SMARCAL1 does not impair its helicase activity. In contrast, mutations within the HARP2 domain entirely abolish SMARCAL1's ability to anneal an RPA-coated plasmid substrate. These findings indicated that HARP2 is essential for SMARCAL1's DNA-binding, ATPase, and annealing helicase functions, while HARP1 may play a more supportive role in facilitating SMARCAL1 activity (18). This finding is consistent with our intra-species domain analysis. Furthermore, 3D alignment of the models predicted by AF3 indicated that the truncated human SMARCAL1 (htSMARCAL1), containing the fused HARP domain, aligns closely with the wild-type human SMARCAL1 (hwSMARCAL1), with the exception of the HARP1 domain. Additionally, our analysis revealed that the fused HARP domain of htSAMRCAL1 completely aligns with the HARP2 domain of hwSMARCAL1 (Figure 7A). This suggests that the htSAMRCAL1 resembles hwSMARCAL1 but without the HARP1 domain. Moreover, the 3D alignment of htSMARCAL1 with the SMARCAL1 from *Melanaphis sacchari* (msSMARCAL1), an invertebrate species, demonstrated a highly identical structure between the two structures (Figure 7B). Collectively, these findings imply that the htSMARCAL1 functions similarly to both the hwSAMRCAL but without HARP1 (18) and the invertebrate SMARCAL1, which naturally possesses a single HARP domain.

Despite these findings, our family segregation data revealed that the gross deletion converting hwSMARCAL1 to htSMARCAL1 likely compromised SMARCAL1 function, leading to the development of SIOD. To address this discrepancy, we assessed the impact of the gross deletion on SMARCAL1 interaction with a virtual DNA replication fork using AF3 modeling. In this assessment, we compared the interactions of hwSMARCAL1, htSMARCAL1, and msSMARCAL1 with the virtual DNA replication fork.

To validate AF3 accuracy in simulating such interaction, we re-modeled the interaction between RecG and a three-way DNA replication fork (PDB 1GM5), for which the interaction has already been determined by X-ray diffraction (35).

Our modeling results demonstrated that AF3 successfully reproduced the interaction between RecG and the three-way DNA replication fork with high confidence, closely resembling the experimental model (Figure 8). In the predicted model, pLDDT scores were greater than 70 for most residues and nucleotides, indicating a high level of confidence in their conformational status. Specifically, for some residues, pLDDT scores exceeded 90, signifying an extremely high confidence in their positions. Conversely, a few residues had pLDDT scores ranging from 50 to 70, suggesting lower confidence in their conformational status. Additionally, disordered regions had pLDDT scores below 50, confirming their disordered nature (Figure 8E).

The 3D structural alignment of the AF3-predicted model with the experimental model revealed a high degree of similarity, validating the capability of AF3 in simulating protein-DNA interactions, such as those involving RecG or SMARCAL1 with a DNA replication fork (Figure 8C). AF3 also accurately predicted the conformations of ADP and Zn^{2+} in their binding pockets, with results highly comparable to those obtained by the experimental method (Figure 8D). Minor misalignments observed between the AF3-predicted and experimental models were attributed to the lower resolution of the experimental structure, which was reported as 3.24 Å (35).

Based on our validation of AF3, we simulated the

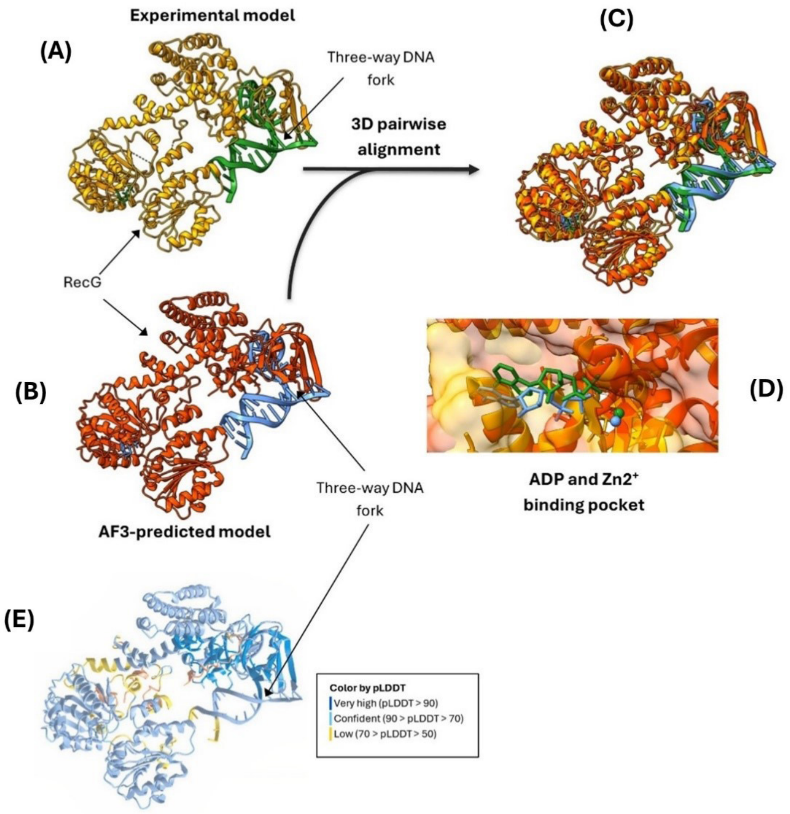

Figure 8. Accuracy of AF3 in predicting protein-replication fork interactions. **(A)** The experimental 3D structure of the interaction between RecG and a three-way DNA replication fork has been previously resolved. **(B)** The AF3-predicted model of this interaction aligns closely with the experimental model, as shown in **(C)**. **(D)** AF3 also accurately reproduces the conformation of ADP and Zn^{2+} within their binding pocket. The conformation of ADP and Zn^{2+} in the AF3-predicted model (blue) closely resembles that in the experimental model (green). **(E)** The AF3-predicted model exhibited high pLDDT scores for most amino acid residues and nucleotides, indicating a high confidence level in the predicted model.

interaction between SMARCAL1 and a virtual DNA replication fork to assess the impact of the gross deletion on this interaction. For the first time, we 3D-modeled the interaction between human SMARCAL1 and a virtual DNA replication fork. After analyzing various replication forks differing in double-stranded (dsDNA) and single-stranded (ssDNA) lengths, we selected a replication fork with a 10-nucleotide dsDNA region and an 8-nucleotide ssDNA region.

The AF3 model revealed that the ATP-dependent helicase domain and the C-terminal helicase directly interact with the dsDNA, while both HARP domains interact with ssDNA (Figure 9A). Additionally, we identified 36 amino acids residues as a helix-strand-strand-helix (HSSH) motif within the ATP-dependent helicase domain, spanning from Phe605 to Ala640, which may contribute to helicase activity by engaging with the newly unzipped dsDNA (Figure 9B).

Moreover, AF3 accurately predicted the conformation of ADP in the ATP binding pocket with extreme confidence, evidenced by a pLDDT score greater than 90. Four amino acid residues—Arg659, Gly461, Lys464, and Gln440—were found to interact with ADP within the ATP binding pocket (Figure 9C).

The pLDDT assessment for the predicted SMARCAL1 model and the substrate DNA replication fork indicated values greater than 90 for most amino acid residues and between 70 and 90 for nearly all remaining residues and nucleotides within the DNA replication fork. For only a limited number of residues near the N-terminal domain and a few nucleotides, pLDDT scores were below 70. The pID for hwSMARCAL1 and DNA fork was 0.9, suggesting that the DNA replication fork conformation relative to hwSMARCAL1 is reasonable (Figure 9D).

A similar simulation was conducted for htSMARCAL1 to determine whether the gross deletion affects the interaction between SMARCAL1 and the virtual DNA replication fork. The AF3 simulation revealed that the gross deletion decreased the pLDDT scores to the range of 50 to 70 for the ssDNA within the DNA replication fork (Figure 9E). This suggests that AF3 had lower confidence in the conformation of ssDNA relative to the HARP domain conformation. This may be due to the gross deletion weakening the interaction between ssDNA and the single fused domain of htSMARCAL1.

However, in a separate simulation of msSMARCAL1's interaction with the virtual DNA replication fork, similar results to those of htSMARCAL1 were obtained (Figure 9F). This indicates that the fused HARP domain in htSMARCAL1 interacts with ssDNA with similar strength as the single HARP domain in msSMARCAL1. Given previous studies that confirm SMARCAL1 with only the HARP2 domain retains its normal helicase, ATPase, and DNA binding functions (18), and considering our 3D

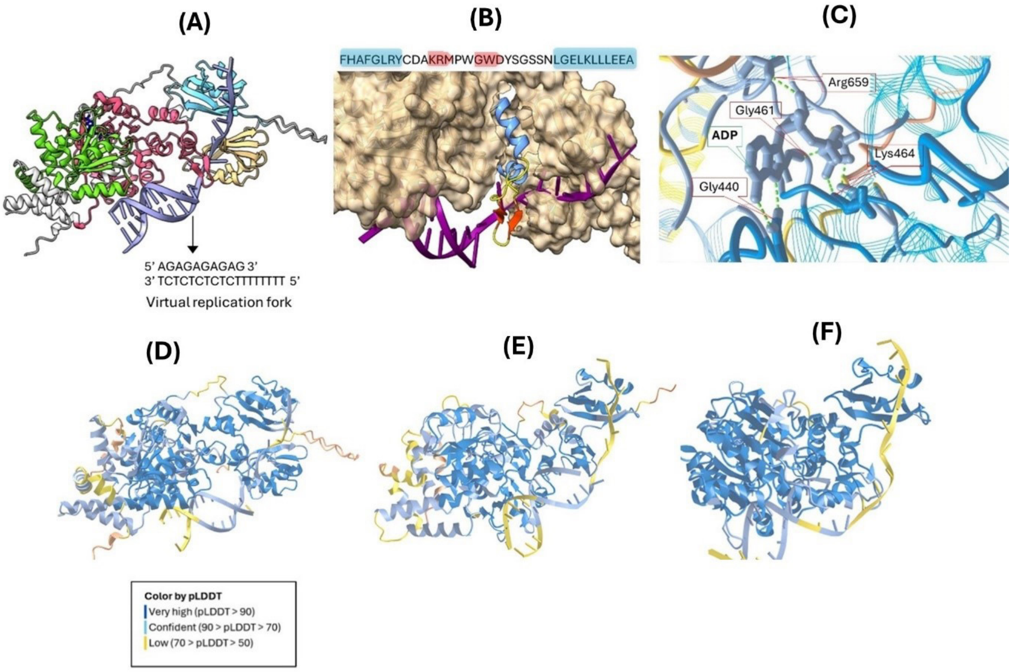

Figure 9. Three-dimensional model of SMARCAL1 interaction with a virtual DNA replication fork. **(A)** The AF3-predicted model demonstrates that the ATP-dependent helicase domain (red) and the C-terminal helicase domain (green) directly engage with double-stranded DNA (dsDNA), while both HARP domains (cyan and golden) interact with single-stranded DNA (ssDNA) within the replication fork. **(B)** A 36-residue HSSH motif within the ATP-dependent helicase domain was identified as a key contributor to SMARCAL1's helicase activity. **(C)** Four critical amino acid residues—Arg659, Gly461, Lys464, and Gln440—within the ATP binding pocket were found to interact with ADP. **(D)** The AF3 model for hwSMARCAL1 indicates that the simultaneous interaction of both HARP1 and HARP2 domains with ssDNA significantly enhances interaction stability (pLDDT > 70). In comparison, the interaction in htSMARCAL1 **(E)** and msSMARCAL1 **(F)** is predicted to be less stable, with pLDDT scores between 50 and 70.

alignment findings that the fused HARP resulting from the gross deletion is identical to the HARP2 domain in human SMARCAL1, we concluded that the cause of SIOD in our proband is not due to impairment of SMARCAL1's helicase, ATPase, or DNA binding functions.

Discussion

SIOD is an infrequent multisystem disorder resulting from genetic abnormalities and should be recognized as a significant diagnosis in individuals presenting with growth retardation and proteinuria (12). It is firmly established that bi-allelic *SMARCAL1* mutations give rise to manifestations of SIOD. *SMARCAL1* serves as a crucial protein for genome integrity remodeling. Deficient *SMARCAL1* cells exhibit collapsed replication forks, cell cycle arrest in the S phase, chromosomal instability, and heightened genomic sensitivity to harmful agents, altering cellular responsiveness to infecting agents affecting replication (13).

Here, we detail a new case involving a large deletion/insertion in *SMARCAL1* identified in one individual, with subsequent investigations revealing the presence of this genetic alteration in her sibling as well. To date, various *SMARCAL1* variants have been identified; variants affecting SMARCAL1 proteins or mRNA depletion, and variants that modify subcellular localization, enzymatic activity, protein levels, or chromatin binding. In contrast, missense mutations impact protein stability, subcellular localization, chromatin binding, and enzymatic activity (22). These results indicate that truncating mutations, splice site mutations, and large deletions/insertions play a more crucial role in the pathogenesis and severity of SOID symptoms. Additionally, due to the distribution of pathogenic and likely pathogenic variants, there is no specific hotspot for *SMARCAL1* mutations from a genetic investigation perspective, and during the analysis phase, especially in WES analysis, all regions should be considered. This aspect may be influenced by the quality of the WES data, the pipelines utilized, and the analysis approach. Nevertheless, when considering missense mutations, particularly those accumulating in the terminal domains covering exons 8 to 17 of the gene, as shown in Figure 5, these variants can be classified into 3 groups according to their position within the conserved C-terminal helicase domain (A468P, I548N, S579L, S579L, T705I, R820H), non-conserved C-Terminal helicase region (R764Q), and nuclear localization signal (R644W, R645C, K647T, K647Q) (23). The majority of pathogenic missense variants identified in the *SMARCAL1* gene exhibit a specific impact on protein function, with the most significant alterations generally involving a loss in ATPase activity (R586W, R644W) and a gain in ATPase activity (K647Q, T705I, R764Q). Furthermore, some missense mutations may hinder DNA binding in the presence of ATP (A468P, R820H) (24-26).

Nonetheless, the variant identified in our study led to a partial deletion of both the HARP1 and HARP2 domains of the wild-type SMARCAL1 (hwSMARCAL1), resulting in a truncated form of SMARCAL1 (htSMARCAL1) that possesses a single fused HARP domain.

After analyzing various replication forks differing in dsDNA and ssDNA lengths, we selected a replication fork with a 10-nucleotide dsDNA region and an 8-nucleotide ssDNA region. Our findings revealed that longer dsDNA regions reduced the pLDDT scores for nucleotides beyond the 10th position, suggesting that SMARCAL1 interacts exclusively with the first 10 nucleotides in the dsDNA region. Similarly, longer ssDNA regions produced comparable results, implying that the HARP domains of SMARCAL1 specifically engage with the initial 8 nucleotides of the ssDNA region.

Prior to initiating the primary modeling, we removed the N-terminal RBD (residues Glu7–Ser37) and the disordered region connecting the RBD to the HARP1 domain (residues Ser38–Ser236). This decision was based on AlphaFold's (AF3) limitations in accurately predicting the structure and interactions of intrinsically disordered regions (37),which lowered model confidence (pLDDT and pID). It has been proposed that the RBD interacts with RPA proteins bound to the ssDNA beyond the eight nucleotides associated with the HARP domains, with the disordered region potentially playing a critical role in this interaction.

A previous study confirmed that dsDNA and ssDNA lengths influence SMARCAL1 binding and ATPase activity in vitro. They demonstrated that a 5-nucleotide ssDNA arm was sufficient for binding and significant ATPase activity, with increasing arm length beyond five nucleotides enhancing SMARCAL1 binding affinity. Furthermore, they reported that a 5-nucleotide ssDNA gap yielded maximum binding and ATPase activity (18). However, our modeling indicated that an 8-nucleotide ssDNA arm is optimal for localization within the HARP domains of SMARCAL1 (Figure 9A). Extending the ssDNA arm beyond eight nucleotides reduced the accuracy of modeling for the additional nucleotides, potentially due to their involvement in interactions with other proteins, such as RPA, during replication fork regression.

We hypothesize that RPA proteins bind to the ssDNA nucleotides beyond the 8^{th} position and interact simultaneously with the RBD domain of SMARCAL1 (removed in our model). This interaction may stabilize SMARCAL1 binding to the replication fork arm. This mechanism could explain why increasing the ssDNA arm length enhances SMARCAL1 binding affinity in vitro.

The AF3-predicted model indicates that htSMARCAL1 closely resembles hwSMARCAL1 but without the HARP1 domain. Furthermore, htSMARCAL1 shows a high degree of structural similarity to the SMARCAL1 found in invertebrate species. A previous study demonstrated that hwSMARCAL1, in the absence of HARP1—equivalent to our htSMARCAL1—retains normal ATPase, helicase, and

DNA binding activities. This suggests that the novel gross deletion observed in our study may not compromise the core functions of SMARCAL1.

Moreover, a recent study has shown that invertebrate SMARCAL1, which lacks the HARP1 domain and closely resembles htSMARCAL1, maintains normal DNA helicase and binding activities but is deficient in the ability to regress DNA replication forks. Thus, based on this previous study, we hypothesize that htSMARCAL1, resulting from the gross deletion, might have lost the capacity for fork regression while retaining helicase activity and DNA binding affinity. However, more experimental studies must be conducted to reveal the exact mechanism by which HARP1 affect SMARCAL1 capacity for fork regression, while retaining of SMARCAL1 activity and binding affinity. The inability to regress DNA replication forks is known to result in genomic instability and can trigger homologous recombination (38,39). However, such recombination could not be identified using common experimental methods such as whole genome sequencing. SMARCAL1 is typically recruited to stalled replication forks to facilitate their regression (40). Replication forks frequently stall due to interactions between the replication machinery and DNA damage, as well as cellular stress responses (41). Therefore, the extent and location of stalled replication forks can vary depending on the level of cellular stress and the nature of DNA damage. Decreasing capacity of SMARCAL1 to replication fork, due to lack of HARP1 domain, might have resulted in different location within genome, representing with different manifestation based on the location of rearrangement. Thus, we presume that patients' clinical manifestation and pathogenicity due to HARP1 domain removal of SMARCAL1, may differ among patients and it possibly could be depended on the location of the resulted rearrangement. This variability in clinical manifestation and pathogenicity is consistent with the observations in our sibling cohort. We observed that the proband's younger sibling has significantly less severe clinical manifestation while sharing the same deletion.

In the developing fetal kidneys, the *SMARCAL1* gene is expressed in various regions such as the ureteric epithelium, stroma metanephric mesenchyme, and during all stages of nephron development. In postnatal kidneys, *SMARCAL1* is found in the epithelial tubules, collecting tubules, and glomeruli including podocytes and endothelial cells. Patients with SIOD exhibited fragmented DNA in renal cells (42,43). Despite early identification of gene defects in renal development stages, clinical manifestations were mainly limited to proteinuria, FSGS, or minimal change disease histopathology with near-normal glomerular filtration rate at diagnosis (44). Our patient, presenting with longstanding proteinuria yet maintaining a normal glomerular filtration rate, corroborates this finding. However, progression to end-stage renal disease could occur spontaneously after the diagnosis of nephropathy, suggested that the severe infantile-onset form of SIOD is linked to *SMARCAL1* null allele, whereas less severe juvenile forms with extended survival are associated with missense mutations (45,46). Nonetheless, a study by Beata S. Lipska-Ziętkiewicz et al found no genotype-phenotype correlation regarding renal defects, with patients having bi-allelic missense mutations showing similar renal survival as those with bi-allelic truncating mutations (47). Despite having the same homogenous deletion-insertion in the *SMARCAL1* gene, our siblings exhibited different renal dysfunctions. Moreover, the presence of ectopic kidneys in both siblings, a rare occurrence within the spectrum of congenital anomalies of the kidneys and urinary tract (5), may highlight an association between the detected variant with ectopic kidneys in SIOD patients.

Our case study underwent an immunological panel assessment following a presentation of esophageal candidiasis, which led to a diagnosis of combined immunodeficiency based on lymphopenia and diminished T and B lymphocyte functions. Although limited data were available for her sibling, his wart presentation was considered a potential sign of immunodeficiency. Immunodeficiency often emerges as a prominent early feature in most reported SIOD cases. Our case study presented lymphopenia alongside reduced lymphocyte function, a common finding in SIOD patients. Approximately 80% of SIOD patients exhibit lymphopenia, while B cell count, and immunoglobulin levels generally remain within normal ranges (47). Additionally, a reduction in immunoglobulin production was observed, although CD19+ levels representing B-lymphocytes were normal. Investigations have indicated that poor B lymphocyte responses in SIOD may result from T cell-dependent B cell activation impairments. Patients with intrinsic B cell defects may experience more severe infectious diseases from encapsulated bacteria compared to those with absent or reduced T cell-dependent B cell responses (47).

Moreover, the study by Bertulli et al on two siblings diagnosed with SIOD unveiled a combined immunodeficiency characterized by profound lymphopenia, thymic output deficiency, defective IL-7Rα expression, disrupted differentiation of B plasma cells, and impaired immunoglobulin production alongside an altered NK-cell phenotype and function. The patients in the previous study presented more severe infectious diseases in comparison to the patients investigated in our research (48). The severity of the disease is directly proportional to the residual activity of the *SMARCAL1* gene (4). However, it is widely acknowledged that gene expression can be influenced by various factors, such as epigenetic elements like DNA methylation and histone modifications, gene redundancy, modifiers, or incomplete penetrance (49). No definite correlations between genotype and phenotype have been reported. It is hypothesized that more severe, early-onset form of the disease has been linked to truncating SMARCAL1 variants that result in a lack of protein production. It is proposed that compound heterozygous missense variants, which produce unstable but present protein, could lead to a milder, nonrenal form of the disease (47). However, there are reports from patients with missense mutations and more severe clinical presentations (50).

Conclusion

This study suggests that the identified gross deletion may contribute to SIOD pathogenesis by impairing DNA replication fork regression and genomic instability. Significant diversity in phenotype was observed among individuals with the same pathogenic variant, even within the same family. An examination of the renal and extra-renal phenotypic range and genotype-phenotype correlations in 34 patients from 28 families highlighted the lack of correlation between genotype and phenotype. Truncating alleles that affect only the C-terminal portion of the protein seem to be associated with a milder phenotype, while nearly all missense mutations affecting the crucial N-terminal helicase ATPase catalytic subdomain led to a distinct SIOD phenotype, with the exception of one mutation. Therefore, the specific intragenic location of the mutation should be carefully considered when predicting phenotype from genotype. Additionally, it is suggested that other genetic factors might modulate the SIOD phenotype through complex oligogenic inheritance.

Authors' contribution

Conceptualization: Mohammad Saberi, Paniz Pourpashang.
Data curation: Morteza Talebi, Ali Ghorbani.
Formal analysis: Azadeh Reshadmanesh.
Funding acquisition: Mohammad Saberi, Paniz Pourpashang.
Investigation: Mohammad Saberi, Paniz Pourpashang.
Methodology: Mohammad Saberi, Paniz Pourpashang.
Project administration: Mohammad Saberi, Paniz Pourpashang.
Resources: Samin Sharafian, Zahra Chavoshzadeh, Masumeh Mohkam.
Software: Arefeh Zahmatkesh.
Supervision: Paniz Pourpashang.
Validation: Paniz Pourpashang.
Visualization: Samin Sharafian, Zahra Chavoshzadeh, Masumeh Mohkam.
Writing–original draft: Mohammad Saberi, Paniz Pourpashang.
Writing–review & editing: Mohammad Saberi, Paniz Pourpashang.

Conflicts of interest

The authors declare that they have no competing interests.

Ethical issues

This case report was conducted in accord with the World Medical Association Declaration of Helsinki. Patient has given us a written informed consent for publication as a case report. Ethical issues (including plagiarism, data fabrication, double publication) have been completely observed by the authors.

Funding/support

The authors declare that they received no funding.

References

1. Liu S, Zhang M, Ni M, Zhu P, Xia X. A novel compound heterozygous mutation of the SMARCAL1 gene leading to mild Schimke immune-osseous dysplasia: a case report. BMC Pediatr. 2017;17:217. doi: 10.1186/s12887-017-0968-8.
2. Ming JE, Stiehm ER, Graham JM Jr. Syndromes associated with immunodeficiency. Adv Pediatr. 1999;46:271-351.
3. Santangelo L, Gigante M, Netti GS, Diella S, Puteo F, Carbone V, et al. A novel SMARCAL1 mutation associated with a mild phenotype of Schimke immuno-osseous dysplasia (SIOD). BMC Nephrol. 2014;15:41. doi: 10.1186/1471-2369-15-41.
4. Jin J, Wu K, Liu Z, Chen X, Jiang S, Wang Z, et al. Whole Exome Sequencing Identified a Novel Biallelic SMARCAL1 Mutation in the Extremely Rare Disease SIOD. Front Genet. 2019;10:565. doi: 10.3389/fgene.2019.00565.
5. Boerkoel CF, O'Neill S, André JL, Benke PJ, Bogdanović R, Bulla M, et al. Manifestations and treatment of Schimke immuno-osseous dysplasia: 14 new cases and a review of the literature. Eur J Pediatr. 2000;159:1-7. doi: 10.1007/s004310050001.
6. Zivicnjak M, Franke D, Zenker M, Hoyer J, Lücke T, Pape L, et al. SMARCAL1 mutations: a cause of prepubertal idiopathic steroid-resistant nephrotic syndrome. Pediatr Res. 2009;65:564-8. doi: 10.1203/PDR.0b013e3181998a74.
7. UniProt Consortium. UniProt: the Universal Protein Knowledgebase in 2023. Nucleic Acids Res. 2023;51:D523-31. doi: 10.1093/nar/gkac1052.
8. Kumar S. SWI/SNF (BAF) complexes: From framework to a functional role in endothelial mechanotransduction. Curr Top Membr. 2021;87:171-198. doi: 10.1016/bs.ctm.2021.09.006.
9. Atkinson J, Gupta MK, Rudolph CJ, Bell H, Lloyd RG, McGlynn P. Localization of an accessory helicase at the replisome is critical in sustaining efficient genome duplication. Nucleic Acids Res. 2011;39:949-57. doi: 10.1093/nar/gkq889.
10. Mirkin EV, Mirkin SM. Replication fork stalling at natural impediments. Microbiol Mol Biol Rev. 2007;71:13-35. doi: 10.1128/MMBR.00030-06.
11. Sogo JM, Lopes M, Foiani M. Fork reversal and ssDNA accumulation at stalled replication forks owing to checkpoint defects. Science. 2002;297:599-602. doi: 10.1126/science.1074023.
12. Schlacher K, Christ N, Siaud N, Egashira A, Wu H, Jasin M. Double-strand break repair-independent role for BRCA2 in blocking stalled replication fork degradation by MRE11. Cell. 2011;145:529-42. doi: 10.1016/j.cell.2011.03.041.
13. Mason AC, Rambo RP, Greer B, Pritchett M, Tainer JA, Cortez D, et al. A structure-specific nucleic acid-binding domain conserved among DNA repair proteins. Proc Natl Acad Sci U S A. 2014;111:7618-23. doi: 10.1073/pnas.1324143111.
14. Cimprich KA, Cortez D. ATR: an essential regulator of genome integrity. Nat Rev Mol Cell Biol. 2008;9:616-27. doi: 10.1038/nrm2450.
15. Zou L, Elledge SJ. Sensing DNA damage through ATRIP recognition of RPA-ssDNA complexes. Science. 2003;300:1542-8. doi: 10.1126/science.1083430.
16. Petermann E, Helleday T. Pathways of mammalian replication fork restart. Nat Rev Mol Cell Biol. 2010;11:683-7. doi: 10.1038/nrm2974.
17. Bansal R, Hussain S, Chanana UB, Bisht D, Goel I, Muthuswami R. SMARCAL1, the annealing helicase and the transcriptional co-regulator. IUBMB Life. 2020;72:2080-2096. doi: 10.1002/iub.2354.
18. Bétous R, Mason AC, Rambo RP, Bansbach CE, Badu-Nkansah A, Sirbu BM, et al. SMARCAL1 catalyzes fork regression and Holliday junction migration to maintain genome stability during DNA replication. Genes Dev. 2012;26:151-62. doi: 10.1101/gad.178459.111.
19. Sayers EW, Bolton EE, Brister JR, Canese K, Chan J, Comeau DC, et al. Database resources of the national center for biotechnology information. Nucleic Acids Res.

2022;50:D20-D26. doi: 10.1093/nar/gkab1112.

20. Ittisoponpisan S, Islam SA, Khanna T, Alhuzimi E, David A, Sternberg MJE. Can Predicted Protein 3D Structures Provide Reliable Insights into whether Missense Variants Are Disease Associated? J Mol Biol. 2019;431:2197-2212. doi: 10.1016/j.jmb.2019.04.009.
21. Schwarz JM, Rödelsperger C, Schuelke M, Seelow D. MutationTaster evaluates disease-causing potential of sequence alterations. Nat Methods. 2010;7:575-6. doi: 10.1038/nmeth0810-575.
22. González-Pérez A, López-Bigas N. Improving the assessment of the outcome of nonsynonymous SNVs with a consensus deleteriousness score, Condel. Am J Hum Genet. 2011;88:440-9. doi: 10.1016/j.ajhg.2011.03.004.
23. Sim NL, Kumar P, Hu J, Henikoff S, Schneider G, Ng PC. SIFT web server: predicting effects of amino acid substitutions on proteins. Nucleic Acids Res. 2012;40:W452-7. doi: 10.1093/nar/gks539.
24. Woods H, Schiano DL, Aguirre JI, Ledwitch KV, McDonald EF, Voehler M, et al. Computational modeling and prediction of deletion mutants. Structure. 2023;31:713-723.e3. doi: 10.1016/j.str.2023.04.005.
25. Wang B, Tian W, Lei X, Perez-Rathke A, Yuan Tseng Y, Liang J. Structure-based Method for Predicting Deleterious Missense SNPs. IEEE EMBS Int Conf Biomed Health Inform. 2019;2019:10.1109/bhi.2019.8834504. doi: 10.1109/bhi.2019.8834504.
26. Bertoline LMF, Lima AN, Krieger JE, Teixeira SK. Before and after AlphaFold2: An overview of protein structure prediction. Front Bioinform. 2023;3:1120370. doi: 10.3389/fbinf.2023.1120370.
27. Sanjeevi M, Hebbar PN, Aiswarya N, Rashmi S, Rahul CN, Mohan A, et al. Chapter 25 - Methods and applications of machine learning in structure-based drug discovery. In: Tripathi T, Dubey VK, editors. Advances in Protein Molecular and Structural Biology Methods. Academic Press; 2022. p. 405–37.
28. Agnihotry S, Pathak RK, Singh DB, Tiwari A, Hussain I. Chapter 11 - Protein structure prediction. In: Singh DB, Pathak RK, editors. Bioinformatics. Academic Press; 2022. p. 177–88.
29. Abramson J, Adler J, Dunger J, Evans R, Green T, Pritzel A, et al. Accurate structure prediction of biomolecular interactions with AlphaFold 3. Nature. 2024;630:493-500. doi: 10.1038/s41586-024-07487-w.
30. Liu W, Xie Y, Ma J, Luo X, Nie P, Zuo Z, et al. IBS: an illustrator for the presentation and visualization of biological sequences. Bioinformatics. 2015;31:3359-61. doi: 10.1093/bioinformatics/btv362.
31. Blum M, Chang HY, Chuguransky S, Grego T, Kandasaamy S, Mitchell A, et al. The InterPro protein families and domains database: 20 years on. Nucleic Acids Res. 2021;49:D344-D354. doi: 10.1093/nar/gkaa977.
32. Meng EC, Goddard TD, Pettersen EF, Couch GS, Pearson ZJ, Morris JH, et al. UCSF ChimeraX: Tools for structure building and analysis. Protein Sci. 2023;32:e4792. doi: 10.1002/pro.4792.
33. Pettersen EF, Goddard TD, Huang CC, Meng EC, Couch GS, Croll TI, et al. UCSF ChimeraX: Structure visualization for researchers, educators, and developers. Protein Sci. 2021;30:70-82. doi: 10.1002/pro.3943.
34. Goddard TD, Huang CC, Meng EC, Pettersen EF, Couch GS, Morris JH, et al. UCSF ChimeraX: Meeting modern challenges in visualization and analysis. Protein Sci. 2018;27:14-25. doi: 10.1002/pro.3235.
35. Singleton MR, Scaife S, Wigley DB. Structural analysis of DNA replication fork reversal by RecG. Cell. 2001 Oct 5;107:79-89. doi: 10.1016/s0092-8674(01)00501-3.
36. Pourpashang P, Esfandiar N, Panjeshahi S, Sharafian S, Mirbehbahani SH. Schimke immuno-osseous dysplasia in a boy with generalized edema; a case report. J Nephropathol. 2024;13:e21481. doi: 10.34172/jnp.2023.21481
37. Ruff KM, Pappu RV. AlphaFold and Implications for Intrinsically Disordered Proteins. J Mol Biol. 2021;433:167208. doi: 10.1016/j.jmb.2021.167208.
38. Atkinson J, McGlynn P. Replication fork reversal and the maintenance of genome stability. Nucleic Acids Res. 2009;37:3475-92. doi: 10.1093/nar/gkp244.
39. Carr AM, Lambert S. Replication stress-induced genome instability: the dark side of replication maintenance by homologous recombination. J Mol Biol. 2013;425:4733-44. doi: 10.1016/j.jmb.2013.04.023.
40. Adolph MB, Cortez D. Mechanisms and regulation of replication fork reversal. DNA Repair (Amst). 2024;141:103731. doi: 10.1016/j.dnarep.2024.103731.
41. Marians KJ. Lesion Bypass and the Reactivation of Stalled Replication Forks. Annu Rev Biochem. 2018;87:217-238. doi: 10.1146/annurev-biochem-062917-011921.
42. Sarin S, Javidan A, Boivin F, Alexopoulou I, Lukic D, Svajger B, et al. Insights into the renal pathogenesis in Schimke immuno-osseous dysplasia: A renal histological characterization and expression analysis. J Histochem Cytochem. 2015;63:32-44. doi: 10.1369/0022155414558335.
43. Baradaran-Heravi A, Cho KS, Tolhuis B, Sanyal M, Morozova O, Morimoto M, et al. Penetrance of biallelic SMARCAL1 mutations is associated with environmental and genetic disturbances of gene expression. Hum Mol Genet. 2012;21:2572-87. doi: 10.1093/hmg/dds083.
44. Pedrosa AK, Torres LF, Silva AC, Dantas AB, Zuntini KL, Aguiar LC. Rare case of nephrotic syndrome: Schimke syndrome. J Bras Nefrol. 2016;38:370-373. doi: 10.5935/0101-2800.20160057.
45. Lou S, Lamfers P, McGuire N, Boerkoel CF. Longevity in Schimke immuno-osseous dysplasia. J Med Genet. 2002;39:922-5. doi: 10.1136/jmg.39.12.922.
46. Elizondo LI, Cho KS, Zhang W, Yan J, Huang C, Huang Y, et al. Schimke immuno-osseous dysplasia: SMARCAL1 loss-of-function and phenotypic correlation. J Med Genet. 2009;46:49-59. doi: 10.1136/jmg.2008.060095.
47. Lipska-Ziętkiewicz BS, Gellermann J, Boyer O, Gribouval O, Ziętkiewicz S, Kari JA, et al; PodoNet Consortium. Low renal but high extrarenal phenotype variability in Schimke immuno-osseous dysplasia. PLoS One. 2017;12:e0180926. doi: 10.1371/journal.pone.0180926.
48. Bertulli C, Marzollo A, Doria M, Di Cesare S, La Scola C, Mencarelli F, et al. Expanding Phenotype of Schimke Immuno-Osseous Dysplasia: Congenital Anomalies of the Kidneys and of the Urinary Tract and Alteration of NK Cells. Int J Mol Sci. 2020;21:8604. doi: 10.3390/ijms21228604.
49. Yusufzai T, Kadonaga JT. HARP is an ATP-driven annealing helicase. Science. 2008;322:748-50. doi: 10.1126/science.1161233.
50. Lipska-Ziętkiewicz BS. Application of genetic testing in steroid-resistant nephrotic syndrome. Kidneys. 2018;7:76-80.